Retrieval of Wind and Total Surface Current Vectors Using Experimental Bidirectional Along-Track Interferometric TanDEM-X Data

Caldarella, Nina; Lopez-Dekker, Paco; Prats-Iraola, Pau; Nouguier, Frederic; Chapron, Bertrand; Zonno, Mariantonietta; Rodriguez-Cassola, Marc

DOI
10.1109/TGRS.2022.3147490

Publication date
2022

Document Version
Final published version

Published in
IEEE Transactions on Geoscience and Remote Sensing

Retrieval of Wind and Total Surface Current Vectors Using Experimental Bidirectional Along-Track Interferometric TanDEM-X Data

Nina Caldarella, Paco Lopez-Dekker, *Senior Member, IEEE*, Pau Prats-Iraola, *Senior Member, IEEE*, Frédéric Nouguier, Bertrand Chapron, Mariantonietta Zonno, and Marc Rodriguez-Cassola, *Member, IEEE*

***Abstract*— Observations of wind and ocean surface velocity vectors by along-track interferometry (ATI) with the synthetic aperture radar (SAR) are not only important for direct applications but also to increase understandings of ocean upper layer mixing, air–ocean interactions, and mapping submesoscale (1–10 km) structures. An experimental bidirectional (BiDi) ATI acquisition mode of TanDEM-X observes with two squinted beams separated by an angle of approximately 13.2° in azimuth on the ground. The baseline is very short, and the along-track interferometric phase (ATI phase) of the ocean surface in the line-of-sight direction of the beams can be interpreted as a total Doppler velocity. The 2-D Doppler velocity field will thus include wind-wave detected motions. In this article, Doppler velocity fields acquired from this experimental acquisition mode are presented. The sequential retrieval of wind vector and total surface current vectors (TSCV) is demonstrated on the BiDi TanDEM-X data. The retrieval algorithm builds on existing geophysical model functions (GMFs) of normalized radar cross section (NRCS) and Doppler velocity. XMOD2 and a GMF based on the Elfouhaily ocean wave spectrum coupled with a Kirchhoff approximation (EOWS&KA) are used. The retrieved wind fields are generally consistent with the European Centre for Medium-Range Weather Forecasts (ECMWF) ERA-5. While the ATI phase errors are small, the retrieved TSCV field looks promising. Acquisitions were located at sea over the tip of the Novaya Zemlya in Russia and over an area near Tromsø, Norway.**

***Index Terms*— Along-track interferometry (ATI), bidirectional (BiDi) synthetic aperture radar (SAR), ocean surface current vectors, TanDEM-X, wind vectors.**

I. Introduction

EXPERIMENTAL along-track interferometric acquisitions in bidirectional (BiDi) mode with TanDEM-X [1] provide opportunities to demonstrate retrieval of 2-D high-resolution surface current fields of the ocean [2]. These data have been long desired to help study small-scale upper ocean processes that play key roles in upper ocean mixing [3] and air–ocean interactions.

The observation of ocean surface currents with synthetic aperture radar (SAR) along-track interferometry (ATI) was demonstrated a long time ago [4]. The along-track interferometric phase (ATI phase) is the along-track phase difference between two SAR images acquired under nearly identical geometry and with a short time lag τ in between. The ATI phase is shifted proportionally to the line-of-sight velocity of the moving target. However, for ocean scenes, this velocity cannot be directly interpreted as a surface current.

It was illustrated using ENVISAT ASAR data that microwave Doppler velocity data encompass high-resolution information about surface currents as well as winds [5]. Traditionally, normalized radar cross section (NRCS) data from broadside-pointing SAR has been exploited to generate high-resolution wind fields. In combination with BiDi ATI phase-derived Doppler velocity data, it may be possible to obtain both high-resolution wind and surface current fields. The Doppler velocity measured by microwave systems is the sum of the Doppler velocity measured without current plus the ocean surface current. In the absence of current, wind-induced ocean surface wave motions produce substantial Doppler velocities that are hereafter referred to as wind-wave-induced artifact surface velocity (WASV) [6], [7]. Wind-generated gravity waves are the dominant drivers of the WASV, with sea state development and swell playing smaller but nonnegligible roles. Ocean surface wind and waves also generate net displacements of water through phenomena such as Ekman drift and Stokes drift that are components of ocean surface currents but are not part of the WASV.

The NRCS can be described by a geophysical model function (GMF) as a function of the wind ten meters above the ocean surface [8]. The wind waves that influence the NRCS also influence the Doppler velocity. Similarly, the Doppler velocity can be described by a GMF [9]. A similar inversion algorithm is presented by Martin *et al.* [7] for X-band SAR measurements. Note that a large number of theoretical GMFs

Manuscript received August 9, 2021; revised December 19, 2021; accepted January 10, 2022. Date of publication January 28, 2022; date of current version March 23, 2022. *(Corresponding author: Nina Caldarella.)*

Nina Caldarella and Paco Lopez-Dekker are with the Department of Geoscience and Remote Sensing, Faculty of Civil Engineering and Geosciences, Delft University of Technology, 2628 CN Delft, The Netherlands (e-mail: r.d.caldarella@gmail.com).

Pau Prats-Iraola, Mariantonietta Zonno, and Marc Rodriguez-Cassola are with the Microwaves and Radar Institute, German Aerospace Center (DLR), 82234 Wessling, Germany.

Frédéric Nouguier and Bertrand Chapron are with the Laboratoire Océanographie Physique et Spatiale LOPS, Institut Français de Recherche pour l'Exploitation de la Mer, 29280 Plouzané, France.

Digital Object Identifier 10.1109/TGRS.2022.3147490

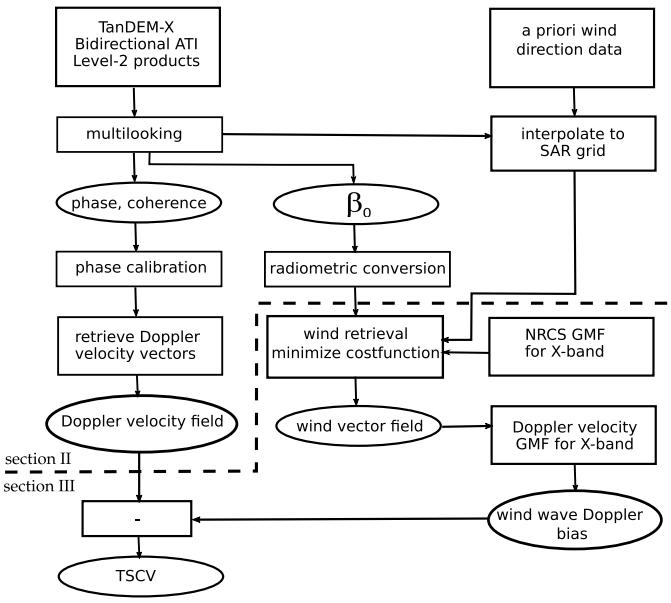

Fig. 1. Data flowchart also indicating the structure of this article. TanDEM-X BiDi ATI data and the European Centre for Medium-Range Weather Forecasts (ECMWF) ERA-5 wind direction data are inputs to the process flow. TSCV and the wind vector are the outputs. ECMWF wind direction is only used to constrain the sign of the solution of the wind vector.

have been developed (e.g., [10]–[12]). Only a few of them have been validated against observations, and this study will help assess the applicability of the model [12].

The BiDi ATI SAR concept was first proposed by Frasier and Camps [13]. It combines two interferometric pairs to generate two separate images in the "fore" and "aft" directions. Later, the concept was demonstrated by Toporkov *et al.* [14] in an airborne campaign. A BiDi ATI SAR has further been used in the airborne wavemill proof-of-concept experiment that aimed at estimating the wind-wave-induced surface velocity for X-band SAR [6].

TanDEM-X and TerraSAR-X are so far the only satellites capable of formation flying with near-optimum ATI baselines, providing sensitivity and coherent imaging of the ATI phase on the ocean [15]. For these unique data, TanDEM-X and TerraSAR-X antennas are squinted in azimuth to the maximum possible angle supported by the antenna [1].

The retrieval of the total surface current vectors (TSCVs) from these data makes a good pilot study for satellite missions using a similar geometry for the observation of ocean surface winds and currents.

Interferometric processing of the data has been done in the German Aerospace Center (DLR), Oberpfaffenhofen, Germany. The available acquisitions with a suitable observation geometry are located over the tip of the Novaya Zemlya in Russia and an area at the coast near Tromsø. The presence of a land area is necessary for phase calibration.

Fig. 1 shows an overview of the research. Section II describes the specificities of the experimental satellite data and the ATI processing of the phase and NRCS. In Section III, a wind vector and TSCV retrieval algorithm for BiDi ATI TanDEM-X data is presented. Results are presented in Section IV and this article closes with the final conclusions in Section V.

II. TanDEM-X BiDi Along-Track Interferometry

A. Concept

A BiDi imaging mode with the TerraSAR-X and TanDEM-X SAR simultaneously images in two directions with one antenna. In this way, two beams are formed, squinted apart as far as possible to an approximate value of 2.2° in the fore and aft directions from the nominal range direction.

In Fig. 2, the geometry of the squinted angles is depicted. On the ground, the along-track beam separation is around 40 km, depending on the angle of incidence of the acquisition. The incidence is steep for the available acquisitions, ranging from 16° up to 23°. In the bistatic StripMap mode, the two satellites image the ocean surface continuously over a period of time to generate the image of a 30-km-wide strip. One satellite operates in the transmit and receive modes, while the other satellite only receives. The first satellite in orbit acquires the master image.

The TerraSAR-X and TanDEM-X orbits are positioned such that the along-track baseline B_{AT} is small enough to provide a coherent image of the ocean surface. We avoid observing in the vertical dimension by minimizing the height sensitivity of interferometry. The height sensitivity of SAR interferometry is commonly described with the height of ambiguity. This is the height in meters for which one phase cycle occurs in the interferogram and it is inversely proportional to the sensitivity. Only data are selected with a large height of ambiguity of 1000 m or above.

The amount of measured phase cycles corresponds to a distance over the period of the interferometric time lag

$$\tau = \frac{B_{\mathrm{AT}}}{2 \cdot v_{\mathrm{orb}}} \tag{1}$$

where B_{AT} is the along-track baseline and v_{orb} is the platform velocity in m/s. The interferometric phase can then be related to a velocity in line-of-sight of the beam

$$\phi_{\mathrm{ATI}} = -2\pi \frac{B_{\mathrm{AT}}}{\lambda} \frac{v_{\mathrm{LoS}}}{v_{\mathrm{orb}}} \tag{2}$$

where ϕ_{ATI} is the interferometric phase of the ATI images in cycles, λ is the radar wavelength (approximately 0.032 m for X-band radar), and v_{LoS} is the velocity in radar line-of-sight in m/s. For each squinted beam, an average of the sea surface motion (v_{LoS}) is projected on the line-of-sight of the sensor. The phase velocity provides an estimate of the first moment of the Doppler spectrum.

With (1) and (2), we can compute the velocity in beam line-of-sight

$$v_{\mathrm{LoS}} = \frac{\phi_{\mathrm{ATI}}}{4\pi} \frac{\lambda}{\tau}. \tag{3}$$

By using a dual-beam configuration, with beams in different directions, along- and across-track components of the Doppler velocity measured in beam line-of-sight can be found using the following geometric relations:

$$v_{\mathrm{at}} = \frac{v_{\mathrm{fore}} - v_{\mathrm{aft}}}{2 \sin(\psi_s)} \tag{4}$$

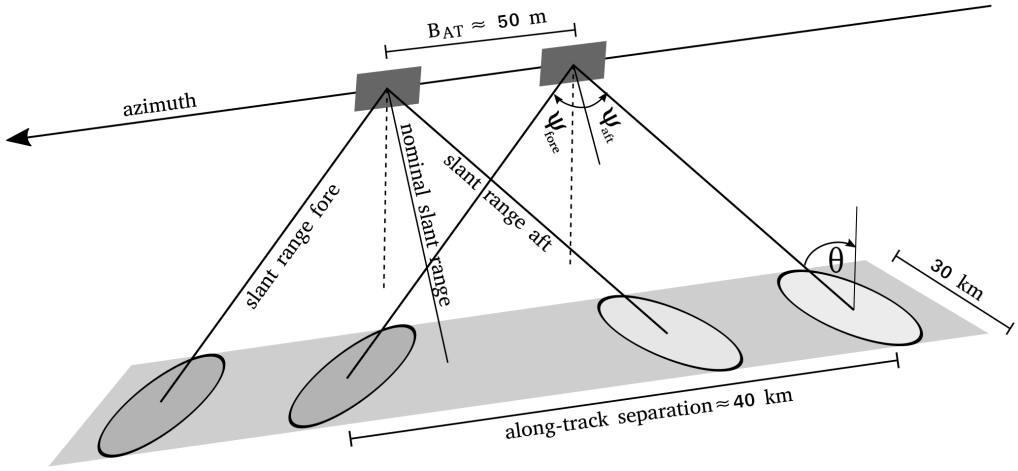

Fig. 2. Schematic overview of the concept and geometry. TanDEM-X and TerraSAR-X have short along-track baselines of around 50 m. The antenna is squinted in two directions where ψ_{fore} and ψ_{aft} may differ slightly and have an approximate value of 2.2°. The angle of incidence θ for the data used in this study ranges from 17° to 22 °. The two satellites image a strip on the ocean surface with a width of 30 km in the StripMap acquisition mode.

and

$$v_r = \frac{v_{\text{fore}} + v_{\text{aft}}}{2\cos(\psi_s)} \tag{5}$$

where v_{at} and v_r are the components of Doppler velocity in along- and across-track (line-of-sight) directions, respectively, and ψ_s is the radar squint angle. This is basically scaling of the beam line-of-sight velocities for the along-track component and an average of the beam line-of-sight velocities for the across-track line-of-sight component. The uncertainty of the across-track line-of-sight component is a factor $\tan(\psi_s)$ smaller than the along-track component (0.04 in this specific case).

If instead of the line-of-sight component, we are interested in the horizontal motion, v_r needs to be scaled with $\sin(\theta)$, where θ is the angle of incidence. As a consequence, the sensitivity in the horizontal plane needs to be scaled with an additional term of $1/\sin(\theta)$. The sensitivity then becomes the following:

$$\frac{\delta v_{\text{xt}}}{\delta v_{\text{at}}} = \frac{\tan(\psi_s)}{\sin(\theta)} \tag{6}$$

where v_{xt} is the Doppler velocity component in the horizontal across-track direction and the other parameters have not changed with respect to their earlier definition.

In the BiDi imaging mode, the azimuth antenna pattern has two main lobes pointing in different directions [1]. The resulting Doppler azimuth spectrum has a large bandwidth. The two components can be separated in the Doppler frequency domain. Each beam has a nonzero Doppler centroid, as a consequence, errors in coregistration will lead to larger phase errors than for the nominal range direction. The noise equivalent sigma zero (NESZ) of BiDi imaging mode is affected by the splitting of the beams, as the intensity of the antenna pattern of each squinted beam is approximately half the intensity of the antenna pattern for a single beam.

A phase ramp is present in the range direction. This becomes a phase offset in the interferogram [16]. Due to a difference in Doppler rate introduced by the physical Doppler, there will thus be an additional azimuth shift in the data. This would need to be corrected in the SAR focusing process.

TABLE I

RELEVANT ACQUISITION PARAMETERS AND CONDITIONS OF DATASET A: THE DOPPLER FIELD HAS BEEN ANALYZED; DATASET B: WIND VECTOR AND TSCV HAVE BEEN ANALYZED; AND DATASET C: WIND HAS BEEN ANALYZED. ALL THE ACQUISITIONS HAVE AN ASCENDING ORBIT

	A	B	C
Location	Novaya Zemlya	Novaya Zemlya	Tromsø
Date	13.09.13	22.08.13	04.09.13
Incidence angle	15.6-18.6°	15.6-18.6°	19.5-23.2°
Squint angle	2.20, -2.24°	2.20, -2.24°	2.20, -2.24°
Time lag	0.004 s	0.006 s	0.003 s
PRF	1475 Hz	5900 Hz	5810 Hz
Polarization	VV	VV	VV
Resolution (rg x az)	4.5 x 19.2 m	4.5 x 19.2 m	6.8 x 19.5 m
Height of ambiguity	1191 m	1182 m	2307 m
ECMWF mean wind speed	4.7 m/s	5.5 m/s	2.1 m/s
ECMWF mean wind direction (w.r.t. north)	-142.1°	9.7°	2.2°
ECMWF mean wind direction (w.r.t. range)	-59.4°	89.1°	90.2°

B. Data and Calibration

1) Location and Conditions: The data have been selected based on the requirements of small baselines and the absence of sea ice. There are two over Novaya Zemlya (Russia) and one located near Tromsø (Norway) that meet these requirements. Table I gives the acquisition parameters of the data.

The location of the Novaya Zemlya datasets is shown in Fig. 3. Dataset A, which was acquired in this location (Table I), was preliminarily processed in [17], but radiometric calibration was not performed. Due to the missing calibration,

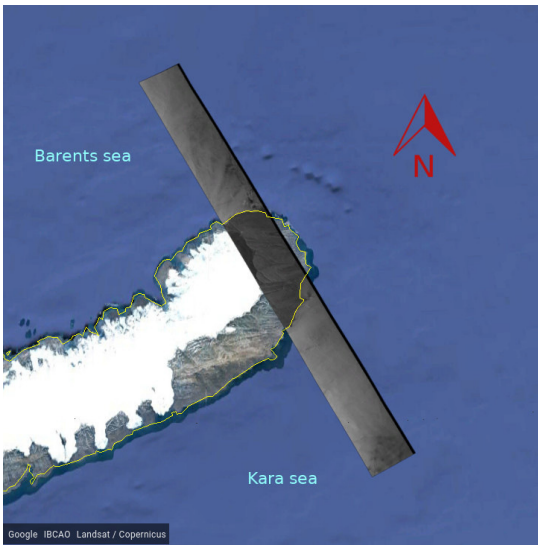

Fig. 3. BiDi ATI acquisition over the Barents Sea and Kara Sea, with the tip of Novaya Zemlya. The latitudes of the image vary between 75.5°N and 78.2°N and the longitudes of the image vary between 63.5°E and 70.9°E. The width of the strip is 30 km.

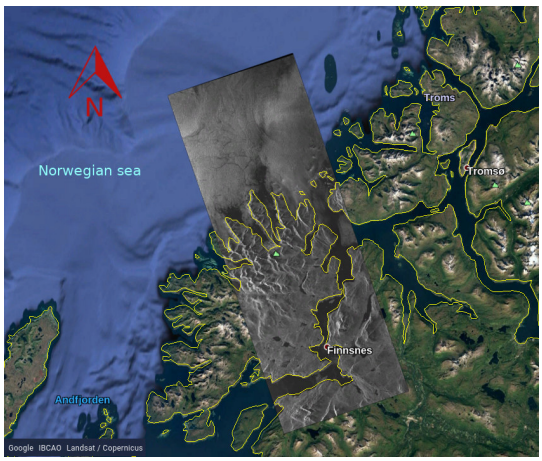

Fig. 4. BiDi ATI acquisition at the coast near Tromsø. The latitudes of the image vary between 68.9°N and 70.3°N and the longitudes of the image vary between 17.7°E and 18.6°E. The width of the strip is 30 km.

dataset A remains unused for retrieval. Dataset B (Table I) was calibrated. ECMWF ERA-5 wind data with a temporal resolution of 3 h and a spatial resolution of 30 km were analyzed for the same acquisition time and locations.

The predominant current at the Barents Sea is the extension of the northward Norwegian Current, which has velocity values ranging from 0.15 up to 0.4 m/s [18]. In the Novaya Zemlya acquisition strip, the water mixes with Arctic Ocean water and is, therefore, colder than the Norwegian Current, and consequently, currents are weaker. In surface current simulations of the Kara Sea [19], it is seen that during spring/summer, there is a very weak anticyclonic circulation and significant inflow from the Barents Sea, while in autumn, currents become stronger and are predominantly along the coast of Novaya Zemlya. Tidal amplitudes are relatively low [20]. Therefore, tidal currents are expected to be weak: no more than 20 cm/s and generally below 2 cm/s [19].

Fig. 4 shows the location of the acquisition over Tromsø. Table I gives the acquisition parameters for dataset C from Tromsø. This dataset was calibrated and ECMWF wind was analyzed.

2) Level-2 Product Data: Interferometric processing of the data with the experimental SAR processor (TAXI) [21] in the DLR outputs the level 2 products of Novaya Zemlya, as shown in Fig. 5. The product includes amplitude data, coherence data, and an interferogram. The high phase values left of the land appear to be ambiguities originating from the mountains near the coast.

The difference between fore look and aft look of the NRCS in the decibel scale is given in Fig. 5(b). After smoothing, geophysical features are found in the image of the NRCS diversity. The mean diversity at sea is 0.2 dB. Notice how the values lie around zero. Consider a GMF, as, e.g., XMOD2 [8]. This value is typical for cross-wind conditions when the nominal range direction is at 90° with the wind. Notice also how the NRCS diversity, which is assumed to correlate with the wind, shows very similar features as the interferogram in Fig. 5.

The mean absolute difference between the interferogram of the fore beam and the aft beam, averaged over sea, gives a value of 0.41 rad. Following (2), we find a value of 0.164 m/s for the mean absolute Doppler velocity diversity at sea.

In the Tromsø dataset in Fig. 6, the NRCS values also turn out very low and there is a phase offset between the fore beam and the aft beam. Topographic features can be seen on the land areas causing layover, which should be avoided in phase calibration. The layover effect is a radar imaging effect that makes tall features appear distorted toward the near range. Low reflection at sea is seen where there are no waves. In this image, the NRCS average over the land area is −16.59 dB, while the NRCS over sea is −15.78 dB. The backscatter ratio between land and sea is close to unity. The small difference between signal on land and at sea indicates that chances to see contributions on the land areas originating from scatterers at sea are high. This would cause errors in the phase calibration.

3) Radiometric Calibration: The amplitudes of BiDi ATI data have been radiometrically calibrated in TAXI with the relation $\beta_0 = k_s \cdot |\mathrm{DN}|^2$, where DN are digital numbers and k_s is the calibration factor [22]. σ_0 is derived from β_0 by means of projection to the ground range with

$$\sigma_0 = (\beta_0 - \mathrm{NEBN}) \sin(\theta_{\mathrm{loc}}) \tag{7}$$

where NEBN is the noise equivalent beta naught. When multiplied with the sine of the local incidence angle θ_{loc}, this becomes the NESZ.

The signal-to-noise ratio of BiDi TanDEM-X is 3.7 dB lower than that of nominal StripMap images [1]; therefore, the NESZ is 3.7 dB higher than for nominal TanDEM-X. Nominal TanDEM-X typically has the NESZ of around −20 dB [22]. The NESZ for BiDi TanDEM-X then follows from SNR = NRCS − NESZ when all three quantities are expressed in decibels and this gives us an NESZ value of −17 dB. The lower SNR is the result of splitting the antenna into two beams. Dataset C of Tromsø has a mean NRCS of −15.2 dB on land, whereas nominal TanDEM-X images with

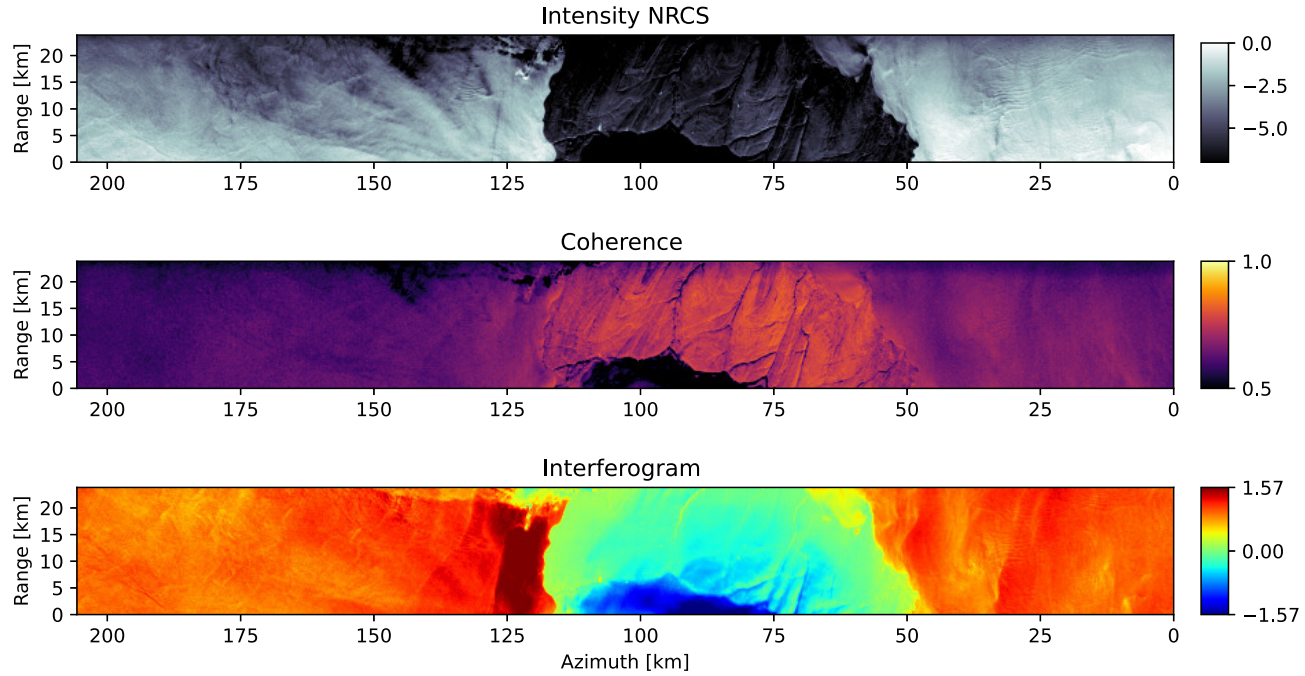

(a)

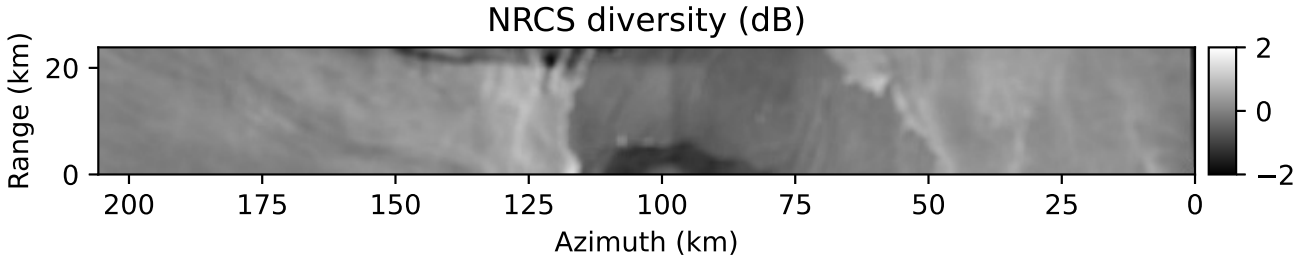

(b)

Fig. 5. Dataset B. The intensity is calibrated, corrected with 6-dB offset, and expressed in NRCS (m^2/m^2) in decibel scale. (a) Level-2 products. In far range, the low coherence is a result of a lower SNR due to the roll-off of the antenna pattern. Low coherence on land is due to ice melt. The high phase values left of the land are azimuth ambiguities. (b) Difference between fore look and aft look of the NRCS in decibel scale smoothed with a window length of 91 samples to about 2-km azimuth resolution.

a similar acquisition geometry and time show a mean NRCS of −9 dB. There appears to be an offset of roughly between 6 and 7 dB. By forward modeling the NRCS using the ECMWF wind data for dataset C of Tromsø at sea and XMOD2, a similar offset between measured NRCS and XMOD2 output values is found. This calibration offset is corrected by adding a constant value between 6 and 7 dB.

4) Phase Calibration: Before the phase offset between the beams was calibrated for dataset B, residual topography had to be removed from the interferograms using the DEM included in the data product multiplied with the interferometric height sensitivity. Dataset A did not have residual topography to correct. We do this because our calibration routine calculates an average offset from zero. Thus, nonzero phase due to topography is unwanted in the calibration.

The offset in the ATI phase between the fore beam and aft beam originates from the sum of errors from residual topography, radar noise, and coregistration errors. Assuming that these errors account for a constant offset between the beams, a methodology is adopted to correct for a phase offset. Given that the ATI phase should be zero on land, the correction is conducted by means of estimating the offset from 0 on land for each beam weighting each point with the coherence to avoid including areas of noisy phase to the estimation. The offset is computed as follows:

$$i_{\text{offset},b} = \sum_{j=1}^{M} W_j \cdot i_{\text{land},b,j} \tag{8}$$

where b is the beam number (1 for fore and 2 for aft), $i_{\text{offset},b}$ is the phase offset in the fore or aft beam, W_j is a weight given to each pixel, and $i_{\text{land},b,j}$ is the interferometric phase of points on land in complex notation. Areas with layover are excluded.

The differences between mean and modal offsets for each beam for Novaya Zemlya do not exceed 0.5°, which implies that the distribution of phase offset is close to normal. This justifies the assumption of a correction with a constant bias estimated from a normal distribution. Considering the offset

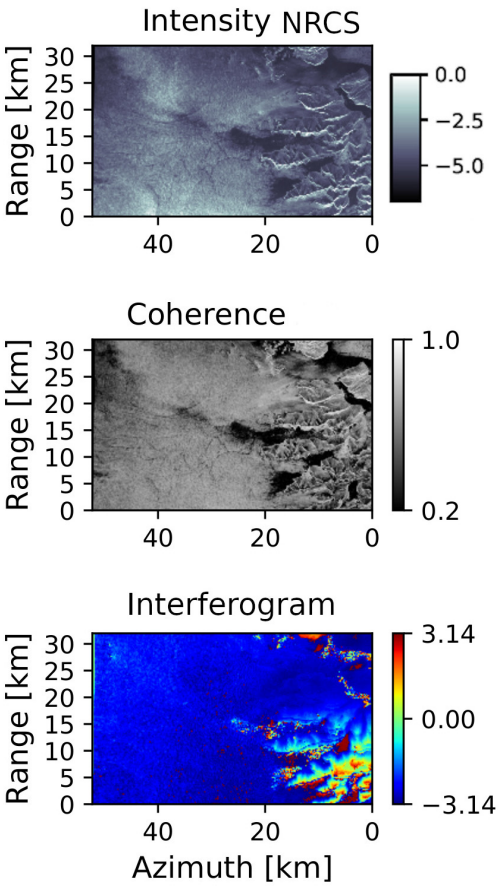

Fig. 6. Level-2 products of the aft look of dataset C near Tromsø. The land consists of high fjords. The layover effect can be seen in the intensity image on the mountains. In the fjords, the coherence is low and intensity is low, where the water is most likely without any wind waves.

between mean and modal phase offset as the calibration error, one finds a Doppler velocity error of about 0.01 m/s.

However, for the case of Tromsø the difference between mean and modal phase offset is 3.9° and 8.9° in the fore beam and aft beam, respectively. These values are much higher than the values seen for Novaya Zemlya. Since the distribution of phase offsets is not Gaussian, the calibration method is unsuitable for this dataset. Therefore, for dataset C, the Doppler velocity is not further analyzed. This decision can also be explained by interpreting the difference between mean and modal phase offset as phase errors that are propagated to the Doppler velocity for each beam when scaled with $\lambda/(\pi\tau)$ following from (3). The resulting velocity errors in the fore beam and aft beam are 0.26 and 0.55 m/s, respectively. The resulting across-track line-of-sight Doppler error is 0.39 m/s following from (5) and the along-track Doppler error is 3.51 m/s following from (6).

Due to the squinted geometry, there will be an additional baseline in line-of-sight direction. This baseline introduces a deterministic error to the 2-D velocity field. Expressed in the radial velocity, the additional error can be calculated with the following expression:

$$\Delta v_r \approx v_r \frac{2 \cdot \psi_s \Delta R_0}{B_{\mathrm{AT}}} \tag{9}$$

where ΔR_0 is the slant range difference in zero Doppler. The effect of this additional baseline is an apparent amplification of the across-track velocity with an even component of true Doppler that is caused by across-track currents and wind. This effect causes an amplification of the along-track velocity with an odd component of true Doppler. The effect has been corrected in the processing by adding an extra temporal baseline term [see (10)].

Using the values of dataset B (Table I) and ΔR_0 of 742.6 m, a value of $\Delta v_r = 1.39\ v_r$ is found. This bias is corrected for by adding an extra temporal baseline term of the form

$$\tau_e = \frac{\Delta R_0 \tan\left(\psi_{s,\mathrm{fore}}\right)}{2 \cdot v_s} \tag{10}$$

where v_s is the satellite velocity.

5) Doppler Field: The Doppler field is retrieved from the calibrated ATI phase using the relations described with (3)–(5). The images have been smoothed to a resolution of 1059 m in azimuth and 973 m in range to mitigate the impact of swell. Swell waves can be seen as ripples in the top of Fig. 5.

From the ATI phase of the Novaya Zemlya acquisition of August 22 (Fig. 5), the Doppler field was retrieved with high accuracy. The uniformity of the Doppler field direction [Fig. 7(b)] is indeed very similar to that of the ECMWF wind field (Fig. 13), again an indication of the presence of WASV. High values of Doppler velocity left of the coast are azimuth ambiguities originating from the mountains near the coast of about 900-m altitude. Another argument supporting the identification of these ambiguities is that for dataset A [Fig. 7(a)], acquired at the same geometry and of the same area, but with a different pulse repetition frequency (PRF), no ambiguities are found.

III. Wind Vector and TSCV Retrieval

Provided that there are GMFs for the NRCS and the WASV as a function of the wind vector, the wind vector will first be inverted. Then, the WASV will be modeled and removed from the Doppler components. The NRCS is a function of the azimuth look direction with respect to the wind direction

$$\sigma_0 = \mathrm{GMF}(U_{10}, \phi_a - \phi_0, \theta) \tag{11}$$

where σ_0 the NRCS, U_{10} is the wind speed magnitude 10 m above the sea surface, ϕ_a is the azimuth look direction, and ϕ_0 is the wind direction, for which the north is taken as the reference (Fig. 8).

XMOD2 [8] was used as the GMF for σ_0 in (11). For upwind and downwind directions, XMOD2 generates the highest values of backscattered radar intensity, whereas crosswinds give the lowest values. Increasing wind speeds go with larger values of intensities. The maximum possible diversity of the NRCS occurs when the nominal range is at −125°, −45°, 45°, or 125° angle with the wind vector. Thus, there are four possible solutions for the wind direction.

The WASV is a signed quantity and a function of the same parameters [7]. The fore beam and aft beam receive echoes

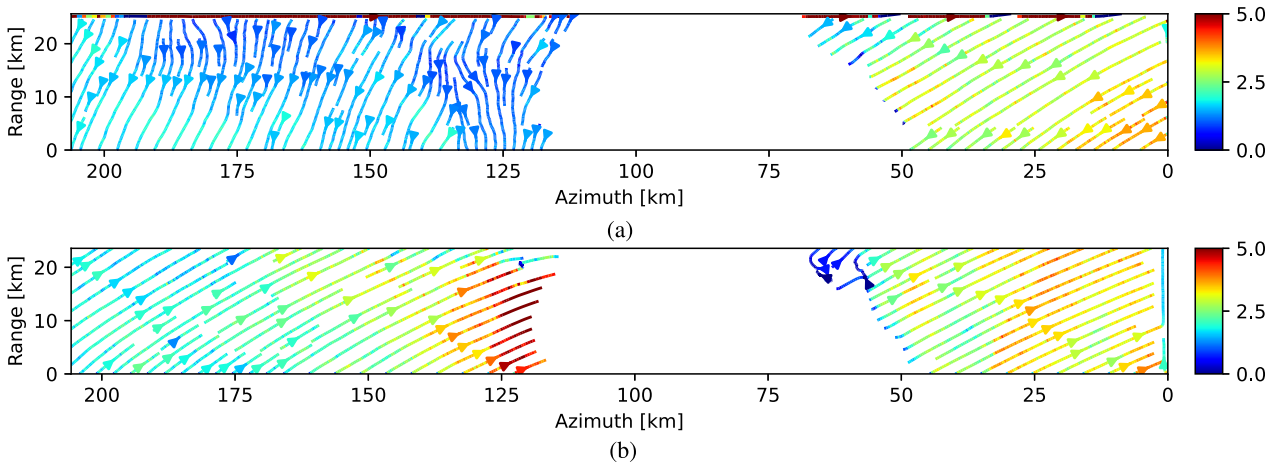

Fig. 7. 2-D Doppler velocity fields over Novaya Zemlya. Using the interferogram data from the two beams and (2), (4), and (5), these vector fields were retrieved. If we only consider the first harmonic of the Doppler GMF, in the absence of current, the Doppler fields would be aligned with the wind. When the wind is aligned with radar line-of-sight of the beam, we would see a maximum or minimum value for the Doppler, and when it is at 90° with radar line-of-sight of the beam, we would see a value of zero for the Doppler. (a) Dataset A. (b) Dataset B. The high values of Doppler seen left from the land are azimuth ambiguities. The radar is looking crosswind. Notice the similarity with the ECMWF winds in Fig. 13.

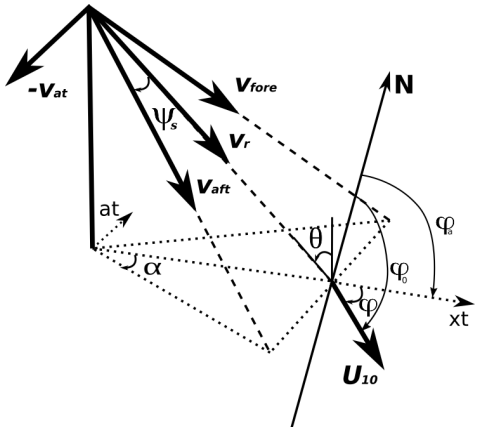

Fig. 8. Sign convention and geometry of the Doppler and wind vectors according to (4), (5), and (11). "at" indicates the along-track axis and "xt" the across-track axis.

from different scattering surfaces for a given patch of ocean. An expression for the GMF may be defined as

$$v_{\mathrm{WASV}} = \mathrm{GMF}(U_{10}, \phi_a - \phi_0, \theta). \tag{12}$$

Fig. 8 shows the geometry of the wind vector, Doppler vectors, and the sign convention. The Elfouhaily ocean wave spectrum coupled with a Kirchhoff approximation (EOWS&KA) [11] is used as a Doppler GMF to calculate v_{WASV}. The Doppler GMF in (12) is zero when the wind is at 90° with the radar line-of-sight and has a maximum or minimum when it is aligned with radar-line-of sight. This is if we consider the first moment of the Doppler in the absence of currents. The Kirchhoff approximation is polarization insensitive, while wave scattering is polarization sensitive. It is therefore expected that the Kirchhoff approximation model for VV data lacks accuracy due to polarization insensitivity [11] except in cross-wind direction, where the Doppler is zero.

Another way to look at the Doppler is by considering small squint angles. Then, the along-track velocity [see (5)] can be rewritten as

$$v_{\mathrm{at}} \approx \left.\frac{\partial v_r}{\partial \psi_s}\right|_{\psi_s=0} = \left.\frac{\partial v_r}{\partial \phi_a} \cdot \frac{d\phi_a}{d\psi_s}\right|_{\phi_a=0} = \frac{1}{\sin(\theta)} \cdot \left.\frac{\partial v_r}{\partial \phi_a}\right|_{\phi_a=0}. \tag{13}$$

It can be seen that an azimuth angle dependence of $\cos(\phi_a - \phi)$ will lead to a Doppler-velocity change in the along-track velocity of the form $\sin(\phi)$. This effect can be seen in Fig. 7(a) and (b), which shows the imprint of a wind field in the retrieved Doppler fields.

The expected diversity modeled with XMOD2 [see (11)] for the mean wind conditions of dataset B given in Table I, and an azimuth beam separation on the ground of 15° and an incidence angle of 17° are −0.04 dB. This is lower than the value of 0.2 dB observed NRCS diversity (Section IV-A2). In this case, it is crosswind, which implies a lower diversity with respect to other wind directions when we consider the sensitivity to directionality of the GMF. Radiometric calibration errors will affect the wind retrievals. To find the right solution for the wind direction among the ambiguities, a constraint is needed.

The expected Doppler velocity diversity modeled with EOWS&KA [see (12)] using the same parameters as in the previous paragraph is 0.160 m/s. This is very close to the observed mean absolute Doppler velocity diversity of 0.164 m/s (Section IV-A2). Indeed, the Doppler velocity measurements are more sensitive than the NRCS. Discrepancies come from calibration errors and are estimated to be of the order 0.01 m/s. Other discrepancies may be attributed to GMF uncertainty.

A. Wind Retrieval Algorithm

The retrieval algorithm that was developed for and demonstrated on TanDEM-X BiDi data is based on the minimization of a cost function (Fig. 9), where the cost function is defined

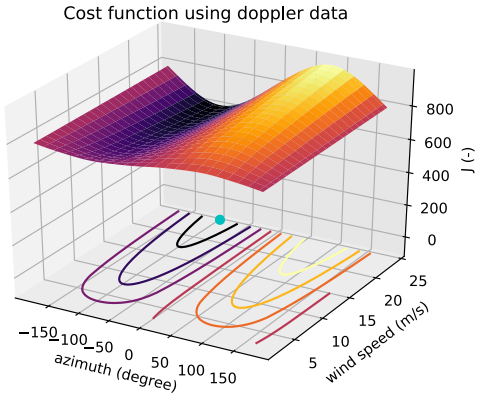

Fig. 9. Illustration showing the principle of the cost function minimization. The blue dot shows the location of the minimum of the cost function in 2-D. Coordinates of this point (wind speed and azimuth) give the values of wind speed and wind direction.

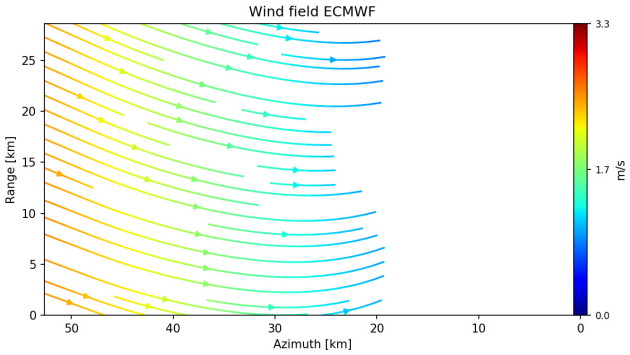

Fig. 10. Wind vector field over the coast near Tromsø resampled to 2-km resolution from the ECMWF ERA-5 Reanalysis model, for the same acquisition time as the BiDi data were taken on September 4. These data have an ensemble standard deviation of approximately 0.4 m/s for wind speed magnitude and 33° for wind direction. The mean wind speed is 2.1 m/s, and the mean wind direction is 90° and thus at crosswind with the radar.

by the squared difference between the NRCS data and a GMF for the backscattered signal from an ocean surface shaped by wind. The cost function can be written as

$$J_{\sigma_0}(U_{10},\phi) = \frac{(\sigma_{0,\text{fore}} - \text{GMF}(U_{10},\phi-\alpha))^2}{\text{Var}\{\sigma_{0,\text{fore}}\}} + \frac{\left(\sigma_{0,\text{aft}} - \text{GMF}(U_{10},\phi+\alpha)\right)^2}{\text{Var}\left\{\sigma_{0,\text{aft}}\right\}} + \frac{(\phi_{\text{ext}} - D)^2}{W_{\text{ext}}} \tag{14}$$

where U_{10} is the wind speed parameter in m/s, $\phi = \phi_a - \phi_0$ is the wind direction parameter relative to across-track look (Fig. 8), σ_0 is the NRCS observation, the GMF is provided as a lookup table, α is the azimuth separation between the beams, and ϕ_{ext} is the wind direction observation from the external data source (ECMWF) with respect to the nominal range direction. Matrix D is filled with a range of wind direction values from $-180°$ to $180°$, repeated along the second dimension and W_{ext} is a tuned weight. W_{ext} is tuned by trial and error to a value of 1×10^{20}. We will find that the first two cost function terms in (14) are very large compared to the third term. Thus, there is an arbitrarily small bias introduced to the wind vector coming from the *a priori* wind direction data.

B. Estimation of the Total Surface Current

The TSCV is given by

$$\mathbf{v}_{\text{TSC}} = \mathbf{v}_{\text{ATI}} - \mathbf{v}_{\text{WASV}} \tag{15}$$

where $\mathbf{v}_{\text{ATI}} = [v_{\text{fore}}, v_{\text{aft}}]$ is the Doppler velocity in each beam following from (3) and $\mathbf{v}_{\text{WASV}} = [v_{\text{WASV,fore}}, v_{\text{WASV,aft}}]$, the WASV found by evaluating a GMF for the Doppler velocity given in (12) with the azimuth angle in the direction of the corresponding beam. v_{TSC} is reconstructed in the along- and across-track directions using (4) and (5).

As a GMF for the WASV, the EOWS&KA was used [12], [23]. The Kirchhoff approximation is known to be effective for steep incidence angles and insensitive to polarization [12]. For data acquired at the incidence angles of 17° and a single VV polarization, polarization effects are expected to be small. Analytical electromagnetic methods were implemented in a software package developed in [12].

The EOWS&KA GMF is evaluated into a lookup table with a resolution of $dU_{10} = 0.1$ m/s, $d\phi = 1°$, and $d\theta = 0.1°$. The choice of these values is based on the approximate accuracy of reference data. The estimation error of wind vectors is usually limited to 0.1 m/s in magnitude and 1° in direction. [24].

In the EOWS&KA model, the Doppler centroid is expressed as a Doppler frequency. The frequency parameter is converted into velocity using the following expression [25]:

$$f_{\text{Dc}} = \frac{2v_r}{\lambda} \tag{16}$$

where f_{Dc} is the Doppler centroid frequency (Hz), v_r is the velocity line-of-sight, and λ is the radar wavelength.

IV. Results

The retrieval algorithm presented in Section III is applied to two datasets presented in Section II. The dataset of Tromsø has been used for tuning of the wind retrieval algorithm. Finally, the Novaya Zemlya dataset of August 22 has been used for the retrieval of the TSCV.

A. Wind Retrieval

1) Tromsø: The results of wind retrieval using XMOD2 (Section II-B3) on the Tromsø dataset are presented and the ECMWF ERA-5 interpolated wind field is shown. To qualitatively assess the results, the two are compared.

The calibration offset that is corrected with a constant value in Section II-B3 gives rise to a calibration uncertainty of roughly 1 dB, which is the same for each beam. This will result in an error of the wind direction and wind speed, depending on the sign and magnitude of the calibration error and the GMF sensitivity.

It is seen that with a sufficiently low weight on the external data term, the solution for wind direction becomes unbiased and only follows the wind direction of ECMWF in a global sense. This is clearly seen by comparing Fig. 10 with Fig. 11. The wind fields have similar values for wind speed. Stronger

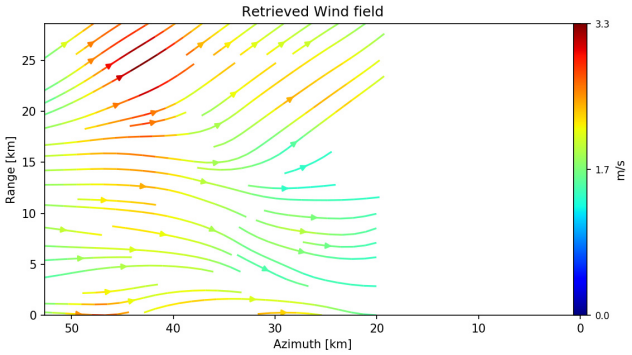

Fig. 11. Retrieved wind field for the Tromsø data using XMOD2 at 2-km resolution. The mean wind speed is 2.9 m/s and the mean wind direction is 78°.

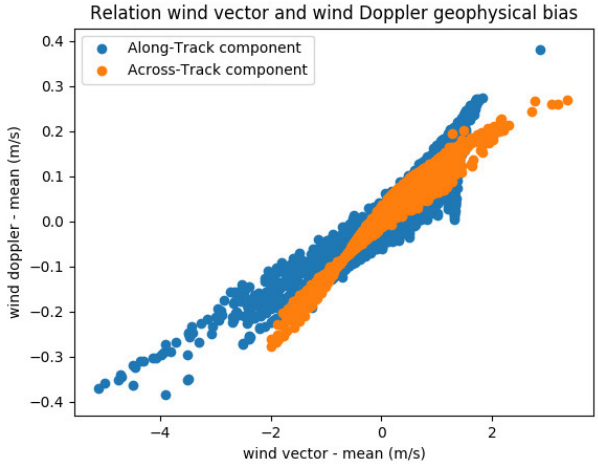

Fig. 12. Correlation of the WASV and wind vector in the along- and across-track directions of the radar. The correlation coefficient lies around 0.1. This implies that for EOWS&KA, the wind vector is scaled with approximately 0.1 to obtain the WASV. Across-track velocity was scaled with $\sin\theta_{\text{nom}}$ to project to the sea surface. The nominal angle of incidence is 20°.

winds are further away from the coast and weaker winds are found near the coast. The wind streamlines curl up for both figures.

ECMWF does not capture local instantaneous effects, as it is an average spatially (low resolution) and temporally (ensemble mean). The retrieved wind in Fig. 11 displays a dark red patch of high winds that are an instantaneous event of high wind speeds. The direction of the wind is slightly more upward for the retrieved winds, but the difference of 11° between ECMWF and retrieved direction is less than the accuracy of ECMWF itself (33°). Other observed differences between retrieved winds and ECMWF are due to the different resolutions of ECMWF and wind retrieval results. A very small bias in the wind retrievals comes from the dependence on *a priori* data. This would be resolved by using a different constraint [7] or detecting wind streaks in the SAR image [26]. The limited validity of the GMF also introduces uncertainty to the retrieval results. It does not capture wave–current interactions, bathymetry effects, or other local modulations of scattering. Close to the coast, local modulations of scattering are more likely to be seen than at open sea. Only the waves that are already developed are captured in the SAR image. Therefore, wind fetch is another source of error. Wind retrieval residuals may also be attributed to surface currents. Studies affirm that scatterometry is current-relative [27]. The observed current-relative winds are commonly found to be of an order 10%–20% different from the Earth-relative winds. Correction of the retrieved wind vector to Earth-relative winds or a joint inversion algorithm would improve the results.

The Doppler velocity calculated with the retrieved wind and GMF for Doppler centroid is expected to relate to the wind linearly with

$$V_{D,\text{wind}} = k \cdot U \tag{17}$$

where v_D is the surface velocity due to intrinsic wind-wave motion in m/s, factor k is found to lie around 0.1, and U is the wind speed in m/s. This factor arises from the GMF. Until today, there has been no consensus on the value of this factor. A correlation graph of the relation of the WASV and wind vector in the along- and across-track directions of the radar (Fig. 12) was generated by subtracting the mean from wind data and WASV. The across-track component of the WASV was multiplied with nominal angle of incidence $\sin\theta_{\text{nom}}$ to project to the sea surface.

2) Novaya Zemlya: The direction of the ECMWF wind field (Fig. 13) is very similar to that of the Doppler field [Fig. 7(b)], suggesting a high correlation between wind and Doppler.

Reasonable agreement is found between the wind direction of ECMWF and the retrieval results (Fig. 14) with a magnitude of retrieved wind 1.7 m/s higher than ECMWF and general agreement in direction as can be seen by comparing Figs. 13 and 14. Note that the retrieved wind is instantaneous and ECMWF a 3-h average, and thus, the values may be quite different. An overestimation of wind vector magnitude might lead to an overestimation of WASV. The local high velocities seen left of the land in the Doppler field are not seen in the inverted wind field.

ATI Doppler data in beam line-of-sight were tested as an input for the same retrieval algorithm. Retrieving a wind vector from the Doppler data implies that we are assuming that all measured Doppler is a consequence of wind, which is contradictory to earlier assumptions. Wind retrieval using the Doppler data was attempted and the direction of the wind field retrieved from Doppler is 45° different from ECMWF in Fig. 13. The discrepancy could be of geophysical and/or nongeophysical origin. A geophysical signal could be any of the geophysical components, and we consider the TSCV to be the sum of: swell waves, Stokes drift, and surface current. A possible nongeophysical signal is errors in the phase calibration of the beams with respect to one another.

B. Total Surface Current Vector

The WASV estimated using the retrieved winds for Novaya Zemlya on August 22 (Fig. 14) is removed from the Doppler components as described in Section III-B. The WASV is lower than the ATI velocity, which can be explained by the presence of a large surface current and a crosswind, for which polarization effects do not play a role. The result

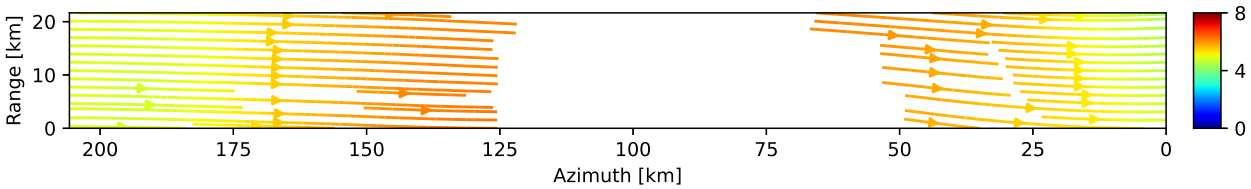

Fig. 13. ECMWF ERA-5 wind vectors 10 m above the sea surface interpolated to roughly a 10-km resolution grid. The mean wind speed is 5.5 m/s and the direction is crosswind relative to the radar.

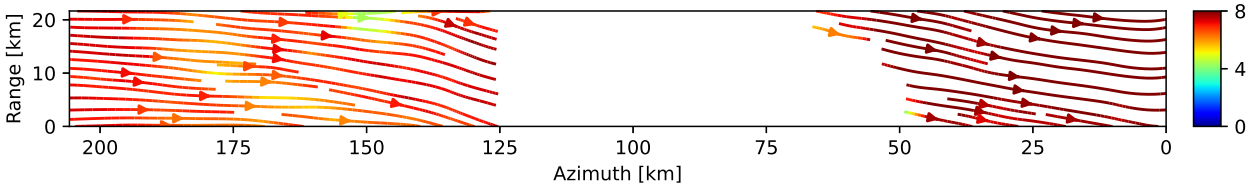

Fig. 14. Retrieved wind field Novaya Zemlya at roughly 10-km resolution. The wind field shows more local features than ECMWF wind field in Fig. 13. The mean wind speed magnitude is 7.2 m/s.

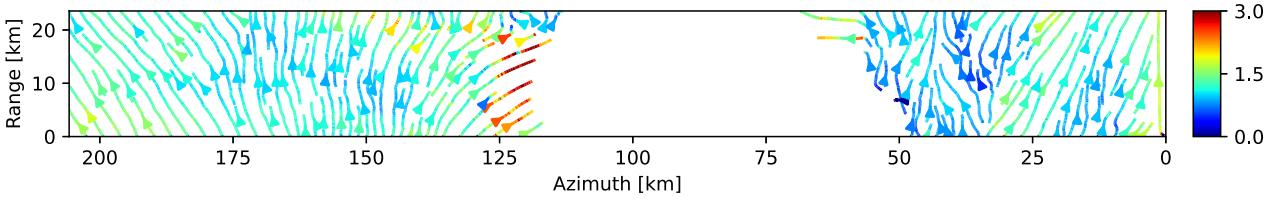

Fig. 15. TSCV field at 250-m resolution. Streamlines run along the coast, which is a characteristic of a current. The extremely high TSCV values are SAR ambiguities.

is a velocity component that relates to the surface motion associated with currents and other components of higher order (Fig. 15). Uncertainty of the resulting TSCV comes from wind retrieval errors, GMF uncertainty, Doppler velocity calibration errors, and a factor 0.04 smaller sensitivity of the along-track direction due to the low diversity. A characteristic of a current is either zero velocity at the coastlines or streamlines along the coast. It is interesting that the results show the latter.

Some agreement is found between the direction of geostrophic currents available on the GlobCurrent application [28] and the direction of the TSCV. This is a geostrophic surface current of 1/3° spatial resolution and weekly temporal resolution inferred from remote sensing data [29]. Errors in this geostrophic surface current may be large due to the coastal location because Ekman components are strong at the surface. Therefore, it is advisable to use a validation dataset that includes the Ekman components [30]. Other shortcomings of these validation data are the lack of wind-driven currents at the surface and the different resolutions. The tidal amplitudes in the region are weak [20]. Nevertheless, for future work, it is recommended that tidal components are also considered using the Tide Model Driver package [31] when attempting this difficult validation of instantaneous surface current measurements in polar areas without oceanic buoys.

Analysis of the divergence of the TSCV and comparison with the divergence of the Doppler velocity field shows a high similarity. Taking the gradient of the phase quantity removes systematic bias from the data. Since the WASV is very smooth relative to the ATI phase, small-scale turbulence is independent of it. This indicates that the absolute current value may not be necessary for the identification of small-scale upper ocean dynamical features, at least in the case of a smooth wind field.

V. Conclusion

Unique experimental TanDEM-X acquisitions in the BiDi mode help assess the performance of ATI at two locations on the Arctic Ocean. The ATI phase calibration was successful at one of the locations and high-resolution 2-D velocity fields could be retrieved.

Anticipated, the 2-D velocity field can display a signature very similar to a wind field. To retrieve the ocean surface currents, a method to retrieve the wind vector and TSCV is applied using GMFs: empirical and, based on the Kirchhoff approximation, an ocean wave spectrum and *a priori* wind direction information.

After applying the necessary corrections to the data, the wind estimated with XMOD2 shows general agreement with atmospheric model data while resolving more local features than the atmospheric model. Shortcomings of the retrievals are calibration errors, limited validity of the GMF, a very small bias due to the use of *a priori* data and winds that are current-relative.

The inversion of 2-D wind vector and TSCV is still found promising because the retrieved TSCV streamlines follow the coast and these streamlines generally follow the same direction as the streamlines in the GlobCurrent application. Full validation of these data is challenging and would require necessary colocated oceanographic data; at exact time, the ATI images were acquired. More systematic acquisitions,

to possibly sample the different tidal phases, would certainly help for future investigations.

More important, while wind vector and TSCV retrieval algorithms have obvious limitations, foremost to rely on mean geophysical models, high-resolution ATI phase field can be more directly exploited. Indeed, ATI phase gradients can be more directly used to identify and study small-scale ocean eddies and filaments, small compared to atmospheric scales. Moreover, systematic large-scale biases are removed, and one may even omit the geophysical retrieval step.

Note that due to the squinted observation geometry, an additional azimuth shift is present in the data that still need to be corrected in the SAR focusing process.

This study provides an experimental base for future investigations in the development of GMFs and the design of satellite missions such as harmony [32] that aim at attaining the long-desired high-resolution characteristics of the upper ocean dynamics.

REFERENCES

[1] J. Mittermayer, S. Wollstadt, P. Prats-Iraola, P. Lopez-Dekker, G. Krieger, and A. Moreira, "Bidirectional SAR imaging mode," *IEEE Trans. Geosci. Remote Sens.*, vol. 51, no. 1, pp. 601–614, Jan. 2013.

[2] N. Caldarella, "Joint retrieval of wind- and total surface current vectors from TanDEM-X bidirectional along-track interferometric data," M.S. thesis, Dept. Geosci. Remote Sens., Delft Univ. Technol., Delft, The Netherlands, 2018.

[3] P. Klein and G. Lapeyre, "The oceanic vertical pump induced by mesoscale and submesoscale turbulence," *Annu. Rev. Mar. Sci.*, vol. 1, no. 1, pp. 351–375, Jan. 2009.

[4] R. M. Goldstein and H. A. Zebker, "Interferometric radar measurement of ocean surface currents," *Nature*, vol. 328, no. 6132, pp. 707–709, Aug. 1987.

[5] B. Chapron, F. Collard, and F. Ardhuin, "Direct measurements of ocean surface velocity from space: Interpretation and validation," *J. Geophys. Res. Oceans*, vol. 110, no. C7, pp. 1–17, Jul. 2005.

[6] A. C. H. Martin, C. Gommenginger, J. Marquez, S. Doody, V. Navarro, and C. Buck, "Wind-wave-induced velocity in ATI SAR ocean surface currents: First experimental evidence from an airborne campaign," *J. Geophys. Res., Oceans*, vol. 121, no. 3, pp. 1640–1653, Mar. 2016.

[7] A. C. Martin, C. P. Gommenginger, and Y. Quilfen, "Simultaneous ocean surface current and wind vectors retrieval with squinted SAR interferometry: Geophysical inversion and performance assessment," *Remote Sens. Environ.*, vol. 216, pp. 798–808, Oct. 2018.

[8] F. Nirchio and S. Venafra, "XMOD2—An improved geophysical model function to retrieve sea surface wind fields from cosmo-sky med X-band data," *Eur. J. Remote Sens.*, vol. 46, no. 1, pp. 583–595, Jan. 2013.

[9] A. A. Mouche *et al.*, "On the use of Doppler shift for sea surface wind retrieval from SAR," *IEEE Trans. Geosci. Remote Sens.*, vol. 50, no. 7, pp. 2901–2909, Jul. 2012.

[10] R. Romeiser and D. R. Thompson, "Numerical study on the along-track interferometric radar imaging mechanism of oceanic surface currents," *IEEE Trans. Geosci. Remote Sens.*, vol. 38, no. 1, pp. 446–458, Jan. 2000.

[11] A. A. Mouche, B. Chapron, N. Reul, and F. Collard, "Predicted Doppler shifts induced by ocean surface wave displacements using asymptotic electromagnetic wave scattering theories," *Waves Random Complex Media*, vol. 18, no. 1, pp. 185–196, 2008.

[12] F. Nouguier, C.-A. Guerin, and G. Soriano, "Analytical techniques for the Doppler signature of sea surfaces in the microwave regime—I: Linear surfaces," *IEEE Trans. Geosci. Remote Sens.*, vol. 49, no. 12, pp. 4856–4864, Dec. 2011.

[13] S. J. Frasier and A. J. Camps, "Dual-beam interferometry for ocean surface current vector mapping," *IEEE Trans. Geosci. Remote Sens.*, vol. 39, no. 2, pp. 401–414, Feb. 2001.

[14] J. V. Toporkov, D. Perkovic, G. Farquharson, M. A. Sletten, and S. J. Frasier, "Sea surface velocity vector retrieval using dual-beam interferometry: First demonstration," *IEEE Trans. Geosci. Remote Sens.*, vol. 43, no. 11, pp. 2494–2502, Nov. 2005.

[15] R. Romeiser, J. Johannessen, F. Collard, V. Kudryavtsev, H. Runge, and S. Suchandt, *Direct Surface Current Field Imaging from Space by Along-Track InSAR and Conventional SAR*. Cham, Switzerland: Springer, Jul. 2010, pp. 73–91.

[16] M. Bara, R. Scheiber, A. Broquetas, and A. Moreira, "Interferometric SAR signal analysis in the presence of squint," *IEEE Trans. Geosci. Remote Sens.*, vol. 38, no. 5, pp. 2164–2178, Oct. 2000.

[17] P. Lopez-Dekker *et al.*, "Experimental bidirectional SAR ATI acquisitions of the ocean surface with TanDEM-X," in *Proc. EUSAR 10th Eur. Conf. Synth. Aperture Radar*, Jun. 2014, pp. 1–4.

[18] R. Sætre and R. Ljøen, "The Norwegian coastal current," in *Proc. Port Ocean Eng. Under Arctic Conditions*. Bergen, Norway: Univ. of Bergen, 1972, pp. 1–22.

[19] I. H. Harms and M. J. Karcher, "Modeling the seasonal variability of hydrography and circulation in the Kara sea," *J. Geophys. Res., Oceans*, vol. 104, no. C6, pp. 13431–13448, Jun. 1999.

[20] B. Gjevik and T. E. N. O. st, "Model simulations of the tides in the Barents Sea," *J. Geophys. Res.*, vol. 99, no. C2, pp. 3337–3350, Feb. 1994.

[21] P. Prats *et al.*, "TAXI: A versatile processing chain for experimental TanDEM-X product evaluation," in *Proc. IEEE Int. Geosci. Remote Sens. Symp. (IGARSS)*, Jul. 2010, pp. 4059–4062.

[22] *Radiometric Calibration TerraSAR-X Data*, Infoterra, Friedrichshafen, Germany, 2008.

[23] T. Elfouhaily, B. Chapron, K. Katsaros, and D. Vandemark, "A unified directional spectrum for long and short wind-driven waves," *J. Geophys. Res., Oceans*, vol. 102, no. C7, pp. 15-781–15-796, Jul. 1997.

[24] W. Tang, W. T. Liu, and B. W. Stiles, "Evaluation of high-resolution ocean surface vector winds measured by QuikSCAT scatterometer in coastal regions," *IEEE Trans. Geosci. Remote Sens.*, vol. 42, no. 8, pp. 1762–1769, Aug. 2004.

[25] S. Wollstadt, P. López-Dekker, F. De Zan, and M. Younis, "Design principles and considerations for spaceborne ATI SAR-based observations of ocean surface velocity vectors," *IEEE Trans. Geosci. Remote Sens.*, vol. 55, no. 8, pp. 4500–4519, Aug. 2017.

[26] J. Horstmann and W. Koch, "Measurement of ocean surface winds using synthetic aperture radars," *IEEE J. Ocean. Eng.*, vol. 30, no. 3, pp. 508–515, Jul. 2005.

[27] A. M. Plagge, D. Vandemark, and B. Chapron, "Examining the impact of surface currents on satellite scatterometer and altimeter ocean winds," *J. Atmos. Ocean. Technol.*, vol. 29, no. 12, pp. 1776–1793, Dec. 2012.

[28] *Globcurrent Project*. Accessed: Dec. 4, 2021. [Online]. Available: http://www.globcurrent.org/

[29] S. Mulet, M.-H. Rio, A. Mignot, S. Guinehut, and R. Morrow, "A new estimate of the global 3D geostrophic ocean circulation based on satellite data and *in-situ* measurements," *Deep Sea Res. II, Top. Stud. Oceanogr.*, vols. 77–80, pp. 70–81, Nov. 2012.

[30] F. Ardhuin, L. Marié, N. Rascle, P. Forget, and A. Roland, "Observation and estimation of Lagrangian, Stokes, and Eulerian currents induced by wind and waves at the sea surface," *J. Phys. Oceanogr.*, vol. 39, no. 11, pp. 2820–2838, Nov. 2009.

[31] *Tmd MATLAB Toolbox*. Accessed: Dec. 4, 2021. [Online]. Available: https://www.esr.org/research/polar-tide-models/tmd-software/

[32] P. Prats-Iraola, M. Pinheiro, M. Rodriguez-Cassola, R. Scheiber, and P. Lopez-Dekker, "Bistatic SAR image formation and interferometric processing for the stereoid Earth explorer 10 candidate mission," in *Proc. IEEE Int. Geosci. Remote Sens. Symp. (IGARSS)*, 2019, pp. 106–109. [Online]. Available: https://ieeexplore.ieee.org/document/8897930, doi: 10.1109/IGARSS.2019.8897930.

[33] P. Prats-Iraola, P. Lopez-Dekker, F. De Zan, N. Yagüe-Martínez, M. Zonno, and M. Rodriguez-Cassola, "Performance of 3-D surface deformation estimation for simultaneous squinted SAR acquisitions," *IEEE Trans. Geosci. Remote Sens.*, vol. 56, no. 4, pp. 2147–2158, Apr. 2018.

[34] H. Li *et al.*, "Up-to-downwave asymmetry of the CFOSAT SWIM fluctuation spectrum for wave direction ambiguity removal," *IEEE Trans. Geosci. Remote Sens.*, vol. 60, pp. 1–12, 2022.

Nina Caldarella was born in Amsterdam, The Netherlands, in 1992. She received the B.Sc. degree in civil engineering and the M.Sc. degree in applied Earth sciences from the Delft University of Technology, Delft, The Netherlands, in 2015 and 2018, respectively. She completed the master's thesis at the Geoscience and Remote Sensing Department, German Aerospace Center, Weßling, Germany.

She was a Visiting Student at the SAR Missions Group, Microwaves and Radar Institute, German Aerospace Center.

Paco Lopez-Dekker (Senior Member, IEEE) was born in Nijmegen, The Netherlands, in 1972. He received the Ingeniero degree in telecommunication engineering from the Universitat Politècnica de Catalunya (UPC), Barcelona, Spain, in 1997, the M.S. degree in electrical and computer engineering from the University of California at Irvine, Irvine, CA, USA, in 1998, under the Balsells Fellowship, and the Ph.D. degree from the University of Massachusetts, Amherst, MA, USA, in 2003, with a focus on clear-air imaging radar systems to study the atmospheric boundary layer.

In 2003, he joined Starlab Barcelona, Barcelona, where he was involved in the development of GNSS-R sensors and techniques. From 2004 to 2006, he was a Visiting Professor with the Department of Telecommunications and Systems Engineering, Universitat Autònoma de Barcelona, Barcelona, where he taught courses on signals and systems, signal processing, communications systems and radiation, and guided waves. From 2009 to 2016, he led the SAR Missions Group, Microwaves and Radar Institute, German Aerospace Center, Weßling, Germany, with a focus on the study of future synthetic aperture radar (SAR) missions, including the development of novel mission concepts and detailed mission performance analyses. Since 2016, he has been an Associate Professor with the Geoscience and Remote Sensing Department, Faculty of Civil Engineering and Geosciences, Delft University of Technology, Delft, The Netherlands. He has been deeply involved in several radar mission proposals, leading the Sentinel-1 SAR Multistatic Explorer mission proposal. He has coauthored 30 peer-reviewed journal articles and over 100 conference contributions in a broad range of topics related to radar remote sensing.

Dr. Lopez-Dekker was a recipient of the Ramon y Cajal Grant to conduct pioneering research on bistatic synthetic aperture radar at the Remote Sensing Laboratory, UPC, in 2006.

Pau Prats-Iraola (Senior Member, IEEE) was born in Madrid, Spain, in 1977. He received the Ingeniero and Ph.D. degrees in telecommunications engineering from the Universitat Politècnica de Catalunya (UPC), Barcelona, Spain, in 2001 and 2006, respectively.

In 2001, he was a Research Assistant at the Institute of Geomatics, Barcelona. In 2002, he was with the Department of Signal Theory and Communications, UPC, where he worked in the field of airborne repeat-pass interferometry and airborne differential synthetic aperture radar (SAR) interferometry. From December 2002 to August 2006, he was an Assistant Professor at the Department of Telecommunications and Systems Engineering, Universitat Autònoma de Barcelona, Barcelona. In 2006, he joined the Microwaves and Radar Institute, German Aerospace Center (DLR), Weßling, Germany, where he has been the Head of the Multimodal Algorithms Group since 2009. He is the responsible and main developer of the TanDEM-X Interferometric (TAXI) processor, an end-to-end processing chain for data acquired by the TerraSAR-X and TanDEM-X satellites, which has been used to demonstrate novel SAR acquisition modes and techniques. He is currently involved in the design and implementation of the ground processor prototypes and end-to-end simulators of ESA's BIOMASS and ROSE-L missions. His research interests include high-resolution airborne/spaceborne monostatic/bistatic SAR processing, SAR interferometry, advanced interferometric acquisition modes, persistent scatterer interferometry (PSI), SAR tomography, and end-to-end SAR simulation. He has coauthored more than 60 peer-reviewed journal articles in these fields.

Frédéric Nouguier received the "Agregation" and M.S. degrees in applied physics from the École Normale Supérieure de Cachan, Cachan, France, in 2005, the M.S. degree in physical methods for remote sensing from the University of Paris Diderot, Paris, France, in 2006, and the Ph.D. degree in physics from the University of Marseille, Marseille, France, in 2009.

He is currently a Research Scientist at the Laboratoire d'Océanographie Physique et Spatiale (LOPS), Institut Francais de Recherche pour l'Exploitation de la Mer (IFREMER), Plouzané, France. He has experience in applied mathematics, physical oceanography, and electromagnetic wave theory and its application to ocean remote sensing.

Bertrand Chapron received the Ph.D. degree in fluid mechanics from Aix-Marseille University, Marseille, France, in 1988.

He is currently a Senior Research Scientist with the Laboratoire d'Océanographie Physique Spatile, Institut Francais de Recherche pour l'Exploitation de la Mer, Plouzané, France. He has been the Co-Investigator or a Principal Investigator in several ESA (ENVISAT RA2, ASAR, and SMOS), NASA, and CNES (TOPEX and JASON) projects. He has contributed to the development of several algorithms for geophysical parameter retrieval from altimeters, radiometers, or synthetic aperture radar (SAR). He is co-responsible for the ENVISAT ASAR-Wave Mode algorithms and scientific preparation for the ENVISAT and S1 wind, wave, and current. Recently, he collaborated in studies that demonstrated the high potential of radiometers for wind retrieval in extreme conditions and the possibility of doing directional ocean waves spectrum from Sentinel-2. He has authored over 80 publications in refereed journals in applied mathematics, physical oceanography (upper ocean dynamics), and electromagnetic wave theory and its application to ocean surface remote sensing.

Mariantonietta Zonno was born in Bari, Italy, in 1986. She received the M.S. degree (Hons.) in telecommunication engineering from the Politecnico di Bari, Bari, in 2011, and the Ph.D. degree from the Scuola Interpolitecnica di Dottorato, Turin, Italy, and the Politecnico di Bari in 2015.

During her Ph.D. studies, she visited the Microwaves and Radar Institute, German Aerospace Center, Weßling, Germany, for eight months. Since 2014, she has been with the SAR Mission Group, Microwaves and Radar Institute, German Aerospace Center. Her research interests include the study of future synthetic aperture radar (SAR) missions' concepts and analysis of the mission performance.

Marc Rodriguez-Cassola (Member, IEEE) was born in Barcelona, Spain, in 1977. He received the Ingeniero degree in telecommunication engineering from the Universidad Publica de Navarra, Pamplona, Spain, in 2000, the Licenciado (M.Sc.) degree in economics from the Universidad Nacional de Educación a Distancia, Madrid, Spain, in 2012, and the Ph.D. degree in electrical engineering from the Karlsruhe Institute of Technology, Karlsruhe, Germany, in 2012.

From 2000 to 2001, he was a Radar Hardware Engineer with CETP/CNRS, Saint-Maur-des-Fossés, France. From 2001 to 2003, he was a Software Engineer with Altran Consulting, Munich, Germany. Since 2003, he has been with the Microwaves and Radar Institute, German Aerospace Center, Weßling, Germany, where he is currently leading the SAR Missions Group. His research interests include radar signal processing, synthetic aperture radar (SAR) end-to-end simulation, SAR processing and calibration algorithms, crisis theory, and radar mission analysis and applications.